MNRAS 000, 1–14 (2024) Preprint 27 May 2024 Compiled using MNRAS LATEX style file v3.0

Weak LyC escape fraction in two $z \sim 7.5$ galaxies: a possible low contribution of relatively bright galaxies during reionization?

Simon Gazagnes,[1]★ John Chisholm,[1] Ryan Endsley,[1] Danielle Berg,[1] Florianne Leclercq[1]
[1]*Department of Astronomy, The University of Texas at Austin, 2515 Speedway, Stop C1400, Austin, TX 78712-1205, USA*

Accepted XXX. Received YYY; in original form ZZZ

ABSTRACT

We present constraints on the escape fraction of ionizing photons ($f_{\rm esc}^{\rm LyC}$) of two $z \sim 7.5$ relatively bright galaxies, GN 42912-NE and GN 42912-SW, to determine their contribution to the Epoch of reionization (EoR). The high-resolution JWST NIRSpec observations reveal these galaxies reside 125 Mpc apart and are separated by only $\sim 0.1''$. GN 42912-NE and GN 42912-SW are relatively massive ($\log(M_\star/M_\odot) \sim 8.4$ and 8.9, respectively), with gas-phase metallicities at 25% solar, $M_{\rm UV}$ magnitudes of -20.4 and -20.9, O_{32} ratios of 3.7 and > 5.5, and β slopes of -1.92 and -1.51, respectively. The Mg II$\lambda\lambda$2796,2803 Å doublet is detected in GN 42912-NE but not in GN 42912-SW, likely due to its higher ionization environment. We constrain $f_{\rm esc}^{\rm LyC}$ in both objects using Mg II and adopting multiple scenarios to accommodate uncertainties regarding the dust attenuation. We establish realistic conservative upper limits of 11% for GN 42912-NE and 6% for GN 42912-SW. These estimates consistently align with $f_{\rm esc}^{\rm LyC}$ trends observed with β, O_{32}, and the Hβ equivalent width at low-z. In GN 42912-NE, the low $f_{\rm esc}^{\rm LyC}$ may be attributed to a significant presence of neutral gas hydrogen within the galaxy, which suppresses the escaping radiation. This scenario may diverge from low-z leakers, typically characterized by depleted neutral gas environment. While these first constraints do not decisively determine the prevalence of a specific reionization model, they suggest a relatively subdued, possibly negligible contribution from these two relatively luminous galaxies to the EoR, and may hint at systematically lower $f_{\rm esc}^{\rm LyC}$ in reionization-era galaxies than anticipated from pre-JWST models.

Key words: galaxies: high-redshift – dark ages, reionization, first stars – galaxies: starburst

1 INTRODUCTION

100 million years after the Big Bang marked the onset of the Epoch of Reionization (EoR), the final significant phase transition in the Universe. During this epoch, the hydrogen gas within the Intergalactic Medium (IGM) existed in a neutral state. However, the emergence of the first astrophysical objects emitted a sufficient quantity of ionizing photons (photons with wavelengths less than 912Å, also known as Lyman Continuum or LyC photons) to reionize all neutral hydrogen within approximately one billion years. This intricate process remains largely enigmatic, as the dominant contributors to the EoR and the mechanisms facilitating the escape of ionizing photons at high redshifts remain unclear.

To gauge the contribution of the primary sources of ionizing photons, it is imperative to determine their ionizing emissivity, i.e., the rate at which they emit photons per unit time and volume. The combined emissivity of all objects must be substantial enough to ionize all hydrogen atoms in the Universe, while accounting for potential recombination events. The emissivity of a source of ionizing photons ($\dot{n}_{\rm ion}$) is derived from the product of the number density of these objects per ultraviolet (UV) luminosity bin (i.e., the relative density of these objects across various UV brightness bins, $\rho_{\rm UV}$), the intrinsic production rate of ionizing photons within the object ($\epsilon_{\rm ion}$), and the fraction of ionizing photons that successfully escape the environment of the sources to traverse the IGM and contribute to hydrogen reionization ($f_{\rm esc}^{\rm LyC}$).

Prior to the James Webb Space Telescope (JWST) era, studies extrapolated post-reionization observations to model reionization and formulate the relevant cosmological models. These models aimed to satisfy specific constraints, such as the opacity of the Cosmic Microwave Background ($\tau_{\rm CMB}$), and observations of damped Lyman-α (Lyα) wings in quasars, which provided insights into neutral gas fractions at $z > 6$ and facilitated explanations for reionization with relatively straightforward predictions.

Among these models, observations have supported two distinct scenarios. One scenario is dominated by a population of faint objects (Finkelstein et al. 2015, 2019; Robertson et al. 2015; Ouchi et al. 2009; Chisholm et al. 2022), while the other posits a population of bright, more massive objects. Although rare, these bright objects boast significantly larger ionizing emissivities (Naidu et al. 2020, 2022; Matthee et al. 2022), consequently playing a dominant role in the ionizing budget. Both of these models were able to reconcile the pre-JWST constraints on the timeline of Reionization and $\tau_{\rm CMB}$.

The successful launch of JWST and the first two years of observations at redshifts greater than 6 have reshuffled the deck entirely. JWST observations have unveiled a plethora of super-early massive galaxies at redshifts greater than 9 (Ferrara et al. 2023; Labbé et al. 2023; Donnan et al. 2023), as well as galaxies at redshifts greater

★ E-mail: gazagnes@utexas.edu

than 6 exhibiting higher ionizing photon production ($\log \epsilon_{\rm ion} \geq 25.5$) (Atek et al. 2024; Simmonds et al. 2024; Endsley et al. 2023a; Prieto-Lyon et al. 2023; Hsiao et al. 2024) and intense star formation activity (Finkelstein et al. 2023; Harikane et al. 2023; Mason et al. 2023; Eisenstein et al. 2023). These findings have profound implications for pre-JWST reionization models. An increase in $\eta_{\rm ion}$ and $\rho_{\rm UV}$ at redshifts greater than 6 results in an overestimation of the ionizing emissivity of the primary ionizing sources in both faint and bright galaxy models, leading, at least on paper, to cosmic reionization ending prematurely and overpredicting $\tau_{\rm CMB}$ (Muñoz et al. 2024).

Yet, thus far, one crucial ingredient has not received the attention it deserves, considering its pivotal role in shaping our understanding of the Universe. As noted earlier, $n_{\rm ion}^{\cdot}$ depends on $f_{\rm esc}^{\rm LyC}$, a notoriously complex quantity to constrain. In the current JWST era, the task of constraining $f_{\rm esc}^{\rm LyC}$ may be pivotal in resolving the ongoing ionizing budget crisis, potentially stemming from a significant reduction in the number of ionizing photons escaping from reionization sources. However, to verify this hypothesis, we must effectively constrain the $f_{\rm esc}^{\rm LyC}$ of high-redshift sources. This is complex because robust constraints on $f_{\rm esc}^{\rm LyC}$ necessitate direct observations below 912Å, which are unfeasible at redshifts greater than 4 due to IGM absorption (Worseck et al. 2014). Hence, our best approach for constraining $f_{\rm esc}^{\rm LyC}$ lies in relying on indirect diagnostics established from lower redshift observations, where direct constraints can be made and compared to other UV and optical properties observable with JWST.

The past decade has seen an exponential growth in the discovery of LyC leaking galaxies at $z < 6$ (Leitet et al. 2013; Borthakur et al. 2014; Leitherer et al. 2016; Izotov et al. 2016b, 2018a, 2016a, 2018b; Vanzella et al. 2015; de Barros et al. 2016; Shapley et al. 2016; Bian et al. 2017; Steidel et al. 2018; Fletcher et al. 2019; Rivera-Thorsen et al. 2017). A significant recent contribution comes from the Low-z Lyman Continuum Survey (LzLCS) (Flury et al. 2022a), which has substantially augmented the number of LyC detections, adding 35 new LyC galaxies at $z < 0.5$ and enhancing the diversity and completeness of the sample. This endeavor has advanced our understanding of ionizing photon escape (Saldana-Lopez et al. 2022; Flury et al. 2022b; Leclercq et al. 2024; Amorín et al. 2024; Chisholm et al. 2022; Bait et al. 2023) and laid the groundwork for establishing LyC diagnostics applicable to high-z studies.

Among the most promising diagnostics for constraining $f_{\rm esc}^{\rm LyC}$ at high-z is the Mg II$\lambda\lambda$2796,2803 Å doublet. The ionization potential of the Mg II lines closely matches that of H I (15 eV versus 13.6 eV), suggesting that Mg II may serve as a tracer for neutral gas density and thereby indirectly infer LyC escape (Henry et al. 2018; Chisholm et al. 2020). Although cosmological simulations have underscored the complexity of the relationship between LyC leakage and Mg II emission (Katz et al. 2022b), observational studies seems to validate the potential of Mg II in tracing ionizing escape. Predictions of LyC escape fraction using Mg II-based approaches from Henry et al. (2018) or Chisholm et al. (2020) closely align with directly-constrained $f_{\rm esc}^{\rm LyC}$ at low-z (Leclercq et al. 2024; Xu et al. 2022, 2023). Building upon these results, a Cycle 1 program (ID: 1871, PI: Chisholm) was granted $\sim$ 17 hours of observations to capture the Mg II emission of 20 reionization-era galaxies in the GOODS-North field and establish the very first indirect $f_{\rm esc}^{\rm LyC}$ constraints of high-redshift galaxies. In this paper, we analyze the JWST Near Infrared Spectrograph (NIRSpec Böker et al. 2023) high-spectral resolution observations of GN 42912, a bright Lyα emitter at $z = 7.5$ originally reported by Finkelstein et al. (2013). Our objective is to establish the first $f_{\rm esc}^{\rm LyC}$ constraints of this reionization-era system and evaluate their relevance in the context of pre-JWST cosmological models and the current ionizing budget crisis.

This paper is organized as follows: Section 2 introduces the observations and reduction strategy of the JWST data. In Section 3, we analyze the SED properties and Mg II, [O III], [O II], and Balmer emission lines of GN 42912. We present the Mg II-based constraints on the $f_{\rm esc}^{\rm LyC}$ in Section 4. In Section 5, we discuss the reliability of these estimates. We compare these constraints to low-z LyC leakers and trends unveiled at low redshift in Section 6. Finally, we consider these $f_{\rm esc}^{\rm LyC}$ constraints and their implications in the context of reionization models and the current status of the field in Section 7. We conclude in Section 8.

Throughout this paper, we use a cosmology with H_0=67.4, and Ω_M=0.315 (Planck Collaboration et al. 2016) and the solar metallicity is defined as 12+log(O/H) of 8.69 (Asplund et al. 2021). All magnitudes are reported as absolute AB magnitudes and the rest-frame wavelengths of emission lines quoted are given in Angstroms (Å) in the vacuum frame using the National Institute of Standards and Technology database (NIST, Kramida et al. 2022). The uncertainties on all measurements and equations include the propagation of all the uncertainties involved in each, using the PYTHON package UNCERTAINTIES (Lebigot 2023).

2 OBSERVATIONS

Here we describe the JWST observations of GN 42912. Section 2.1 describe the JWST Cycle 1 project in which the observations are part of, Section 2.2 and Section 2.3 describe the NIRcam and NIRSpec data reduction, and Section 2.4 presents a general overview of the GN 42912, actually composed of two close-by galaxies.

2.1 JWST Project ID 1871

The JWST Project ID 1871 (PI: Chisholm) selected 20 high-redshift candidates within the GOODS-North (GN) field, with a focus on quantifying the production and escape of ionizing photons from these galaxies and determining how they contributed to reionization. The data was acquired from the JWST (McElwain et al. 2023; Rigby et al. 2023) on February 10, 2023, specifically utilizing the NIRSpec G235H/F170LP and G395H/F290LP grating capabilities. The high-resolution grating configuration of NIRSpec is critical to capture the detailed velocity-resolved profiles of the Mg II$\lambda\lambda$2796,2803 Å emission lines and deduce the neutral gas column density (and associated LyC escape fraction) within star-forming galaxies (Henry et al. 2018; Chisholm et al. 2020).

The MSA observations were strategically centered on a prominent, bright Lyα emitter at $z = 7.5$ in the GN field, as documented in previous studies (GN 42912, Finkelstein et al. 2013; Hutchison et al. 2019). The in-depth Hubble Space Telescope (HST) H-band observations were used to identify potential Mg II emitter targets and pinpoint galaxies with either spectroscopically confirmed (Jung et al. 2020) or photometrically inferred redshifts above 5. The initial target pool, derived from Finkelstein et al. (2015) and Bouwens et al. (2015), comprised 1,036 possible sources. These were further refined using the Complete Hubble Archive for Galaxy Evolution (CHArGE) HST F160W imaging, which boasts a 100 mas spatial resolution. Finally, 20 sources, located within a single MSA footprint of the bright Lyα emitter and meeting specific criteria—photometric redshifts above 5, F160W magnitudes below 28mag, and more than 3σ detections in Spitzer 4.5 μm, were selected. This selection process was pivotal to ensure the galaxies were akin to bright, star-forming galaxies from

the epoch of reionization and were sufficiently bright for detecting the Mg II doublet and other optical nebular emission lines.

The initial selection of 20 targets relied on photometric redshift, which has inherent limitations compared to spectroscopically confirmed redshift. Only 11 of these targets have the Mg II $\lambda\lambda$2796 and 2803Å emission lines falling within the NIRSpec gratings coverage. Among these, GN 42912 stands out with the most robust detection of the Mg II doublet (exceeding 3σ), making it the primary focus of this paper. The next sections provide a comprehensive overview of the data reduction pipeline.

2.2 NIRcam Data Reduction

NIRCam imaging of the GN field was conducted as part of the First Reionization Epoch Spectroscopically Complete Observations (FRESCO, Oesch et al. 2023)). This imaging spanned medium-band filters (F182M and F210M) in the short-wavelength channel and the F444W filter in the long-wavelength channel. The FRESCO imaging aimed for a 5σ detection of a 28.2 mag source, with total exposure times of 4456, 3522, and 934 seconds for the F182M, F210M, and F444W filters, respectively. These NIRCam images served for validating the NIRSpec data reduction and providing insights into the broad-band properties of GN 42912.

The FRESCO NIRCam images were processed following the methodology set out in Endsley et al. (2023b), using the JWST Science Calibration Pipeline (v1.11.3). We employed specific strategies for removing snowball and wisp artifacts, integrating sky flats and wisp templates derived from publicly available data, and took the photometric zero points from Boyer et al. (2022) within JWST_1106.PMAP. The $1/f$ noise and 2D background subtraction in the *_CAL.FITS files is done on an amplifier-by-amplifier basis, utilizing the SEP package (Barbary 2016).

Each *_CAL.FITS file was aligned to the Gaia astrometric frame, referencing the CHArGE HST WFC3/F160W reductions of the GN field. During the pipeline's final stage, all NIRCam mosaics were resampled to a uniform World Coordinate System with a 30 mas pixel^{-1} scale. We then adjusted the individual images to match the point-spread function (PSF) of the F444W filter (the filter with the longest wavelength in our setup) using PSFs empirically defined within the FRESCO mosaics.

Figure 1 presents a composite image (F180M, F210, F444W) of GN 42912. The resolution of the NIRCAM filters can resolve the presence of two spatially resolved components separated by ~ 0.1". We further detail the properties of both components in Section 2.4. In the rest of this paper, we refer as these two components as GN 42912-NE and GN 42912-SW, to denote the one in the northeast and the southwest, respectively.

2.3 NIRSpec Data Reduction

The NIRSpec observations were divided between the G235H and G395H grating configurations. The G235H observations, focusing on the 2550–3500 Å wavelength range cover the Mg II$\lambda\lambda$2796,2803 Å emission lines for sources at redshift between 5.5 and 9.5. Because of its importance for the program's scientific goals, the G235H grating was allocated a longer exposure time: 53,044 s (approximately 14.7 hours) across 36 exposures. In contrast, the G395H grating, covering restframe optical emission lines brighter than Mg II, required significantly less exposure time, 9716 seconds (around 2.7 hours) over 6 integrations. Both configurations operated under the NRSIRS2 readout mode, and the standard three-shutter nod pattern was employed for background subtraction.

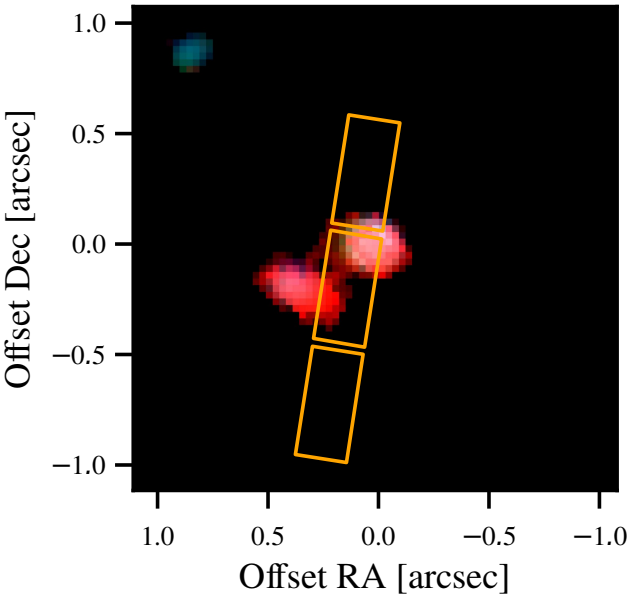

Figure 1. Three-color NIRCam image of GN 42912, with north oriented upwards and east towards the right. The image composite uses the F182M filter for blue, F210M for green, and F444W for red. The dominance of the F444W filter in the composite image, attributed to strong Hα emission, prompted an artificial increase of 30% in the brightness of both the F182M and F210M filters to enhance their visibility. Overlaid in orange are the locations of the three NIRSpec shutters. The spatial resolution of the JWST filters reveals that GN 42912 comprises two companion galaxies, not entirely covered by the rectangular shutters. Further details on GN 42912 are provided in Section 2.4.

Concerning the NIRSpec reduction pipeline, we employed the recently released reference files cataloged under JWST_1227.PMAP, accessible via the CDRS website[1], made available on April 26, 2024. We reduced the NIRSpec data using the MSAEXP v06.17 (Brammer 2023)[2] python code that acts as a wrapper for the default Space Telescope Science Institute data reduction pipeline (we use the JWST pipeline version 1.14.0) while providing a few additional steps. MSAEXP uses the GRIZLI code (Brammer 2019) to drizzle and combine the individual exposures.

We incorporate all exposures into the final data co-addition. However, the distinctive two-component morphology of the GN 42912 system poses challenges for background subtraction. The resulting non-compact morphology in the 2D spectra ismore extended than other single-component sources observed in the context of the same program. As a result, the standard three-shutter nod pattern for subtracting the overall background in each slit is relatively ineffective, as the source overlaps the central band in each nod observation. To address this issue, we implemented a manual slit-based background extraction method, where the overall background is determined using the median of pixels within a sliding window. Appendix A provides details on the implementation of this procedure and the enhancements it enables for the strongest emission lines such as [O III] 5008Å. The final spectrum extraction utilizes a box window covering both emission components.

[1] https://jwst-crds.stsci.edu/
[2] https://github.com/gbrammer/msaexp

Table 1. Properties of the two spatially resolved components in GN 42912 observed under JWST Project ID: 1871 (PI: Chisholm). We refer to these two components as GN 42912-NE (the one in the northeast) and GN 42912-SW (the one in the southwest). The right ascension and declination are the coordinates of the source in the MSA configuration file. The z values are derived as the median redshift and standard deviation of the Hβ, Hγ, [O III] 5008 Å, [O III] 4960 Å, and [Ne III] 3870 Å emission lines. The photometry filters values are in nJy. In the lower section of the table, we provide M_{UV}, derived based on the F125W filter ($\sim$ 1500Å at $z \sim 7.5$), $\log(M_*/M_\odot)$, obtained from BAGPIPES SED fits (Carnall et al. 2018), and β, calculated based on the slope of the F125W and F182M filters.

Property	GN 42912-NE	GN 42912-SW
RA	12:36:37.91	12:36:37.91
DEC	+62:18:08.63	+62:18:08.63
z	7.50165 ± 0.00037	7.49096 ± 0.00077
F182M	124 ± 4	90 ± 5
F210M	123 ± 4	84 ± 6
F444W	266 ± 6	240 ± 8
F606W	-2 ± 3	-6 ± 4
F775W	3 ± 3	3 ± 4
F814W	-6 ± 2	3 ± 3
F850LP	4 ± 8	-16 ± 10
F105W	78 ± 6	34 ± 9
F125W	120 ± 6	74 ± 8
M_{UV} [mag]	-20.37 ± 0.09	-20.89 ± 0.05
$\log_{10}(M_*/M_\odot)$	$8.432^{+0.041}_{-0.032}$	$8.868^{+0.292}_{-0.151}$
β	-1.92 ± 0.08	-1.51 ± 0.16

2.4 General overview of GN 42912

GN 42912 is composed of two close-by galaxies. The redshift of each object, determined from the median redshift and standard deviation of prominent emission lines such as Hβ, Hγ, [O III] 5008Å, [O III] 4960Å, and [Ne III] 3870Å, indicates that the northeast component is at a slightly higher redshift compared to the southwest component (7.50165 versus 7.49096). Both redshifts correspond to luminosity distances of approximately 76294 and 76169 Mpc, respectively, suggesting that the two galaxies are separated by 125 Mpc. Although this distance indicates that the two galaxies are not currently interacting, it does not rule out the possibility of past interactions between them.

It's worth noting that because GN 42912-SW is "in front" of GN 42912-NE, its circumgalactic medium (CGM) gas may absorb some of the escaping radiation, including ionizing photons, from GN 42912-NE. However, the indirect diagnostic based on the Mg II doublet, as utilized in this study, is unlikely to be significantly affected by this scenario. For GN 42912-SW to impact the escaping Mg II, it would require a CGM enriched with Mg II capable of absorbing the incoming radiation. Such a configuration is rare and hence unlikely to influence the observed Mg II features. **THIS NEEDS TO BE REMOVED OR EXPLAINED BY SOMEONE WHO can make THIS BETTER**.

3 GALAXY AND EMISSION LINE PROPERTIES

Here we detail the galaxy and emission line properties of GN 42912-NE and GN 42912-SW. Section 3.1 details the SED-derived properties, and Section 3.2 presents the analysis of the observed emission lines in both galaxies.

3.1 SED properties and β slopes

Utilizing the NIRCam observations, we derive constraints on the Spectral Energy Distribution (SED) properties of GN 42912-NE and GN 42912-SW. The F444W imaging, tracing light up to 4.98 μm (restframe 7500 Å at $z \sim 7.5$), is particularly suited for measuring stellar masses (M_*). The inference of M* involves fitting the SED using the Bayesian Analysis of Galaxies for Physical Inference and Parameter EStimation (BAGPIPES; Carnall et al. 2018) code. BAGPIPES employs updated stellar population synthesis templates from Bruzual & Charlot (2003), a Kroupa & Boily (2002) stellar initial mass function, and incorporates nebular emission through the processing of stellar emission via CLOUDY v17.00 (Ferland et al. 2017). We allow for a broad range of stellar masses, metallicities, and ionization parameters, applying log-uniform priors to all three physical properties. M_* is determined by constraining the underlying restframe UV to optical continuum, as well as the strength of prominent optical lines ([O III] and Hβ).

With BAGPIPES, we infer a $\log(M_*/M_\odot)$ of $\sim$ 8.4 for GN 42912-NE and $\sim$ 8.9 for GN 42912-SW. It is interesting to find such two relatively massive companion early galaxies. The M_{UV}, derived from the F125W filter (restframe 1500 Å), is -20.37 and -20.89 for the NE and SW components respectively. Finally, GN 42912-SW is relatively redder, with a β of -1.51 as compared to -1.92 for its NE companion. We note that the β slopes, derived from the photometry (F125W - F182M), have values consistent with their M_{UV}, and fall within the trend M_{UV}-β trend from Bouwens et al. (2014).

3.2 Emission lines

Here we outline our methodology for measuring the emission line properties of GN 42912-NE and GN 42912-SW. Our analysis focuses on the [O III] 5008Å, [O III] 4960Å, [O II] 3727-3279Å, Hβ, Hγ, and Mg II 2796-2803Å, crucial for deriving constraints on the relative and absolute escape fraction of ionizing photons (see Section 4). These lines are all detected at a significance level of $> 3\sigma$ for the NE component. However, in the SW component, we do not detect [O II] 3727-3279Å and Mg II 2796-2803Å, indicating a potentially higher ionization degree in this galaxy. Figure 2 shows the G235H + G395H combined spectrum (top panel) along with the 2D and 1D extracted spectra for each of the lines of interest, distinguishing between lines detected in both galaxies and those detected only in GN 42912-NE.

We employ a single Gaussian profile to fit each line in our analysis. A separate paper will delve into a more sophisticated fitting approach involving the combination of two Gaussian profiles for strong line, aimed at inferring the outflow properties of each object (Saldana-Lopez, in prep). For our current analysis, we find that using a single Gaussian profile is sufficiently accurate to replicate the observed profiles, and thus we do not explore models combining multiple Gaussian profiles. The fits for each line are displayed in 2.

In cases where we do not detect emission lines in GN 42912-SW, we establish an upper limit on the fluxes of these lines by integrating the spectrum error across the same line width observed for the NE component.

We calculate the equivalent widths (W_λ) for all lines by using a continuum taken as the median flux within a ± 5,000 km s^{-1} feature-free interval on both sides of the lines.

The emission line measurements for GN 42912-NE and GN 42912-SW are reported in 2. Using the flux measurements, we derive a moderate O_{32} ratio for the NE component (3.7), and a lower limit of $\sim$ 5.5 for the SW component.

In terms of the Balmer decrement, in GN 42912-SW, we derive a H_γ/H_β ratio of 0.466, close to the theoretical expectation of $\sim$ 0.468 for an H II region at T = 10,000K and n_e = 500 cm^{-3} (the electron density is derived from [S II] lines, see Stephenson in prep). This ratio

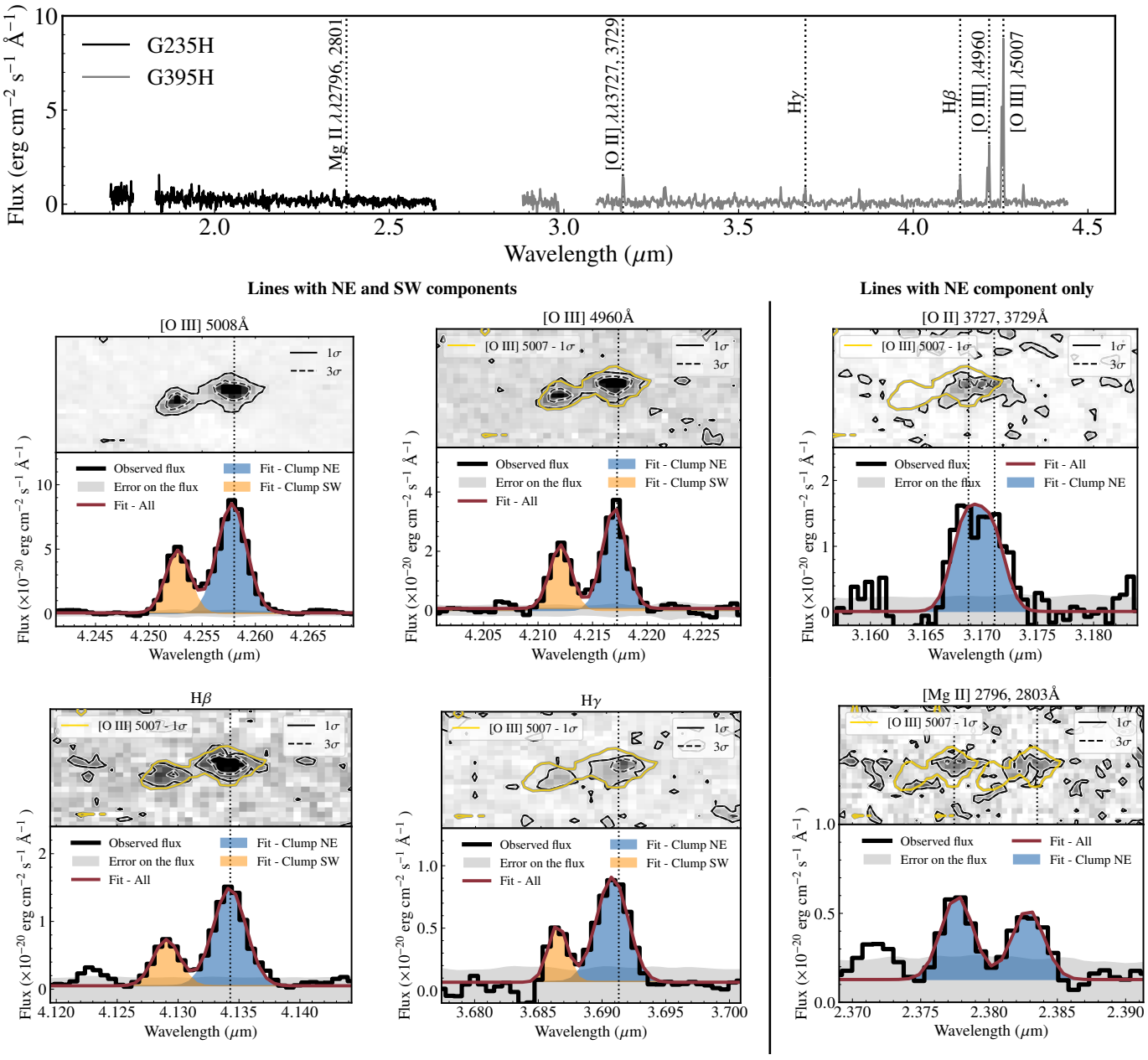

Figure 2. Overview of the spectrum and emission lines of GN 42912-NE and GN 42912-SW. The top panel displays the combined G235H and G395H JWST observations. Below, we present each emission line analyzed in this work, categorizing lines detected in both GN 42912-NE and GN 42912-SW (left part) and lines detected only in GN 42912-NE (right part). Each panel features the 2-D spectrum at the top with the 1 and 3 σ contours, along with overlaid contours from the [O III] 5008Å lines. At the bottom of each panel, observed fluxes are depicted in black, with orange representing the fit to the component of GN 42912-SW, blue representing the fit of the component of GN 42912-NE, and red indicating the total fit combining both. Cases where the lines from GN 42912-SW are not detected include only the fit from the NE galaxy.

indicates a relatively dust-free nebular environment, which contrasts with the relatively dusty continuum suggested by photometry with $\beta \sim -1.5$. In GN 42912-NE, we find a non-physical (under typical Case B assumptions) Balmer ratio for GN 42912-NE. H_γ/H_β is ~ 0.54, hence slightly larger, albeit within 1σ, of the theoretical dust-free value.

Balmer "anomalies" have recently been identified in high-z objects. For example, Cameron et al. (2023) noted a H_α/H_β ratio significantly ($> 1\sigma$) smaller than expected without dust extinction in GS-NDG-9422, a $z \sim 5.943$ galaxy, while (Topping et al. 2024) found notably higher H_γ/H_β and H_δ/H_β values in RXCJ2248-ID at $z = 6.11$. These deviations from the theoretical predictions are currently regarded as "anomalies" and recent studies have proposed different scenarios to elucidate them (Yanagisawa et al. 2024; Scarlata et al. 2024). These scenarios involve unique environments that depart from the typical Case B assumptions and may include Balmer self-absorption (Scarlata et al. 2024) or optically-thick excited H I clouds (Yanagisawa et al. 2024). Understanding the origin of Balmer "anomalies" is important for accurately determining the characteristics of these galaxies, yet this effort lies beyond the scope of our

present analysis. Nonetheless, within the context of our study, Balmer decrement remains critical for correcting the influence of dust on the nebular emission lines. Since a clear model to disentangle dust extinction from other physical processes affecting our H_γ/H_β values is currently lacking, we adopt two distinct approaches for our analysis. In the first scenario, we assume both objects are depleted of dust, thus considering the observed flux values as intrinsic (hereafter, this case is referred to as no-dust-case or NDC). Alternatively, in the second scenario, we correct for dust in the nebular emission lines using the β values as proxies for the E(B-V) extinction (hereafter referred to as β-dust-case or βDC). To estimate the dust extinction E(B-V) from β, we relation we use is equation 7 of Chisholm et al. (2022). By default, we employ an SMC dust extinction law, while also exploring the impact of different extinction laws throughout the paper, such as the one proposed by Reddy et al. (2016), derived from a large dataset of 933 far-UV observations of Lyman Break Galaxies at $z \sim 3$. We further discuss these dust scenarios and assumptions in Section 5.1.

We estimate the O/H abundance in GN 42912-NE and GN 42912-SW (needed in the next section) utilizing the R_{23} empirical metallicity diagnostics from Curti et al. (2020) where the relation between R_{23} and 12+log(O/H) is given as

$$\log(R_{23}) = 0.527 - 1.569 \times x - 1.652 \times x^2 - 0.421 \times x^3 \quad (1)$$
$$\text{with } x = 12 + \log(O/H) - 8.69,$$
$$R_{23} = \frac{F_{corr}([O\,II]\lambda\lambda 3727,3729 + [O\,III]\lambda 5007 + [O\,III]\lambda 4960)}{F_{corr}(H_\beta)}.$$

F_{corr} represents the dust-corrected flux values based on Table 2. For GN 42912-NE, we find R23 = 9.5±0.9 and 12+log(O/H) = 8.07±0.15 in the NDC case, and R23 = 9.6±1.2 and 12+log(O/H) = 8.07±0.18 in the βDC. Given the absence of difference in the central value, we report in 2 the value calculated in the βDC because of the larger uncertainty.

For GN 42912-SW, the [O II]$\lambda\lambda$3727,3729 doublet is not detected. Yet, we find that using the reported upper limit or assuming $F_\lambda = 0$ only marginally influences the final 12+log(O/H) estimate by 0.01. Further, using either the NDC or the βDC case does not influence the final estimate. Similarly as for GN 42912-NE, we report in 2 the most value with the largest uncertainty such that we take hereafter 12+log(O/H) = 8.09 ± 0.25.

In the next section, we detail the two Mg II-based strategies to derive an estimate and an upper limit on the escape fraction of ionizing photons in GN 42912-NE and GN 42912-SW, respectively.

4 THE MG II ESCAPE FRACTIONS OF GN 42912-NE AND GN 42912-SW

In this section, we outline our methodology for computing the Lyman continuum escape fractions (f_{esc}^{LyC}) for GN 42912-NE and GN 42912-SW utilizing the Mg II $\lambda\lambda$2796,2803 Å doublet lines. This Mg II doublet has been suggested as a reliable indirect indicator of LyC escape fraction (Henry et al. 2018), owing to its low ionization potential close to that of hydrogen. This characteristic not only makes it a valuable tracer of neutral gas but also less susceptible to the IGM opacity compared to Lyα, which is directly impacted by H I in the IGM. While a recent simulation-based study from Katz et al. (2022b) has raised some concerns regarding the use of Mg II as a LyC tracer (these concerns being discussed in Section 5.2), several observational studies have demonstrated a close correspondence between direct f_{esc}^{LyC} measurements at ~ 912Å and indirect estimates based on the Mg II 2796-2803Å emission lines (Chisholm et al. 2020; Xu et al. 2023; Leclercq et al. 2024). In this study, we explore two approaches for calculating f_{esc}^{LyC} from these Mg II lines: the doublet ratio method (Section 4.1) and using photoionization models (Section 4.2).

Table 2. Emission line properties in GN 42912. Fluxes (F_λ) are in 10^{-20} erg cm^{-2} s^{-1} Å^{-1} and equivalent widths (W_λ) in Å. The lower section of the table provides properties derived using the line measurements.

Properties	GN 42912-NE		GN 42912-SW	
	F_λ	W_λ	F_λ	W_λ
[O III] λ5007	289 ± 6	428 ± 45	139 ± 5	205 ± 23
[O III] λ4960	92 ± 5	137 ± 18	53 ± 4	79 ± 11
Hβ	49 ± 2	72 ± 12	19 ± 2	28 ± 9
Hγ	26 ± 5	42 ± 13	9 ± 3	14 ± 8
[O II] λ3727	41 ± 7	51 ± 12	< 13	-
[O II] λ3729	37 ± 5	47 ± 11	< 13	-
[Mg II] λ2796	14 ± 3	10 ± 3	< 9	-
[Mg II] λ2803	12 ± 3	8 ± 3	< 9	-
$R_{Mg\,II}$	1.19 ± 0.33		-	
O_{32}	3.70 ± 0.40		> 5.47	
Hγ/Hβ	0.540 ± 0.087		0.466 ± 0.167	
R_{23}	9.6 ± 1.2		< 11.8	
12+log(O/H)$_{R_{23}}$	8.05 ± 0.18		8.09 ± 0.25	

4.1 Doublet ratio method

When the observed Mg II emission lines do not show prominent absorption signatures, one can assume that collisions dominate the Mg^+ excitation. In such a scenario, the intrinsic flux ratio of the Mg II 2796Å and 2803Å emission lines is the ratio of their emissivities, which is 2. This ratio (hereafter R(Mg II)) is confirmed by CLOUDY photoionization modeling done in (Henry et al. 2018). In the scenario where the excitation is dominated instead by photon absorption, the emission flux ratio is set by the ratio of the Einstein A coefficients. Both Mg II 2796 and 2803 lines have similar A21 values, so R(Mg II) would come closer to 1 instead of 2.

Chisholm et al. (2020) showed that, in the optically thin regime, one can use the variation of the R(Mg II) values to infer the neutral hydrogen column density, which in turn provides a constraint into the relative absorption of the LyC photons by the H^0 gas. Such an approach is possible because (1) in the optically thin regime, resonant radiative transfer effects on the Mg II lines are negligible and (2) the Mg^0 and Mg^+ phases overlap with H^0, so a column density of Mg^+ can be transformed into H^0 under some assumption on the Mg/H abundance in the galaxy.

A robust Mg^+ to H^0 conversion requires accurate estimates of the depletion fraction of Mg and of the Mg/H abundance. Accurately determining the fraction of Mg that is depleted into dust is complex, and even more complex for reionization-era galaxies where the number of studies on the topic remains scarce. For consistency with previous studies using a similar approach, we assume a depletion fraction of 27% based on Jenkins (2009). As noted in Chisholm et al. (2020), there exists a substantial scatter for the depletion factor, yet, the depletion most only depends on the ionization for the highly ionized galaxies Guseva et al. (2019).

Regarding the Mg/H abundance, since both oxygen and magnesium are α elements primarily produced by core-collapse supernova, the Mg/O value should not appreciably vary, so we can estimate the Mg/H abundance from the observed O/H abundance and using a solar O/Mg abundance of 12.3 (Asplund et al. 2021).

Chisholm et al. (2020) showed that, under these assumptions, the H I column density can then be approximated as

$$N_{\rm H\,I} = -2 \times 10^{13} {\rm cm}^{-2} \frac{\rm H}{\rm O} \ln({\rm R}/2). \quad (2)$$

From the estimate of $N_{\rm H\,I}$, one can derive a relative escape fraction, $f_{\rm esc}^{\rm rel}$, representing the amount of escaping LyC photons solely based on the quantity of neutral hydrogen and disregarding the influence of dust within the galaxy.

$$f_{\rm esc}^{\rm rel}({\rm LyC}) = e^{-N_{\rm H_0} \times \sigma_{\rm phot}}. \quad (3)$$

To correct for the ionizing photons absorbed by dust, we calculate the absolute escape fraction $f_{\rm esc}^{\rm abs}$ accounting for the reduction in the relative escape fraction due to the expected dust attenuation at 912Å:

$$f_{\rm esc}^{\rm abs}({\rm LyC}) = f_{\rm esc}^{\rm rel} \times 10^{-0.4{\rm E(B-V)k(912Å)}}, \quad (4)$$

where E(B-V) is the line-of-sight dust extinction and k(912Å) is the predicted dust attenuation from the chosen dust extinction law at 912Å. As a small disgression, we remind that most direct and indirect measurements of $f_{\rm esc}^{\rm LyC}$ reported in the literature correspond to the $f_{\rm esc}^{\rm abs}$(LyC) and are line of sight dependent, as our observations only allow us to trace the photons escaping towards us. Yet in practice, one must contain the overall (i.e., angle-averaged) $f_{\rm esc}^{\rm LyC}$ to constrain the reionization process. Since the LyC escape is highly anisotropic (Gazagnes et al. 2020; Saldana-Lopez et al. 2022), transforming line-of-sight constraints into global constraints is not trivial but one can in practice use statistically significant sample of galaxies with $f_{\rm esc}^{\rm LyC}$ constraints to derive the desired angle-averaged quantity.

The doublet ratio method, which has been shown to produce LyC escape fraction estimates consistent with direct constraints in low-z galaxies (Chisholm et al. 2020; Xu et al. 2023; Leclercq et al. 2024), is only applicable to galaxies that have detections of the Mg II 2796 and 2803 Å lines. Hence, in this work, we only apply this method to GN 42912-NE.

To derive $N_{\rm H\,I}$ using Equation 2, we use the O/H abundance derived from the R23 ratio, reported in Table 2. We obtain a $N_{\rm H\,I}$ of $(8.9 \pm 5.4) \times 10^{16}$ cm^{-2}. Using either the NDC or βDC scenarios does not influence this result.

The corresponding $f_{\rm esc}^{\rm rel}$ based on $N_{\rm H\,I}$ is 0.57±0.21. Physically, this means that the amount of neutral hydrogen absorbs approximately 43% of the escaping LyC radiation. This is relatively low as compared to samples of low-z leakers, most of which have $f_{\rm esc}^{\rm rel} \sim 1$ (see further discussion in Section 5).

In the NDC scenario, where we assume that the galaxy is completely devoid of dust, $f_{\rm esc}^{\rm rel}$ is also $f_{\rm esc}^{\rm abs}$ since no attenuation is expected at 912Å. In the βDC scenario, we derive $f_{\rm esc}^{\rm abs}$ using Equation 4 and E(B-V) values transformed from β using Equation 7 from Chisholm et al. (2022). To account for potential impacts of the dust extinction law, we consider the SMC extinction curve (Gordon et al. 2003) and the extinction curve from Reddy et al. (2016) (hereafter referred to as R16). We select these two laws because their extinction curves significantly differ in the UV, providing us with a means to estimate the typical uncertainty in the choice of the dust extinction. We obtain $f_{\rm esc}^{\rm abs}$(R16) of 0.12±0.05 and $f_{\rm esc}^{\rm abs}$(SMC) of 0.16±0.06. These estimates suggest a relatively weak LyC leakage from GN 42912-NE when accounting for the combined attenuation of hydrogen and dust.

The Doublet method comes with a notable caveat: its reliability hinges on the validity of the optically thin regime where the ratio effectively traces $N_{\rm H\,I}$. However, when the observed ratio deviates from this optically thin scenario (i.e., R(Mg II) closer to 1), resonant radiative transfer effects become non-negligible, introducing a bias in the relationship from R(Mg II) to $N_{\rm H\,I}$. This discrepancy might explain the substantial systematic error observed when employing the Doublet method in simulations (Katz et al. 2022b), wherein $f_{\rm esc}^{\rm LyC}$ predictions derived from Mg II substantially overpredict the true $f_{\rm esc}^{\rm LyC}$ as the latter decreases.

For GN 42912-NE, with R(Mg II)$\sim$ 1.2, we likely diverge from the optically thin regime, suggesting that our estimates might be considered as a strict upper limit rather than a central value. We discuss this aspect further in Section 5.

4.2 Using photoionization models

Henry et al. (2018) established a robust correlation between the intrinsic flux of Mg II and the extinction-corrected flux of [O III]5008Å and [O II]3727-3729Å, offering an alternative procedure for predicting $f_{\rm esc}^{\rm LyC}$ compared to the doublet ratio method. Additional, with this method, we can derive upper limits on $f_{\rm esc}^{\rm LyC}$ even when the Mg II doublet remains undetected. Consequently, we employ this method for both GN 42912-NE and GN 42912-SW.

The photoionization model approach builds upon the quadratic relationship between the intrinsic flux ratio of Mg II/[O III] λ5008 and the O_{32} ratio, initially established by Henry et al. (2018) and extended by Xu et al. (2022). Given the moderate O32 ratio observed in our galaxies, we adopt coefficients derived under the ionization-bounded scenario and a metallicity of $\log_{10}(Z/Z_\odot) \sim -0.5$, aligning with the gas-phase metallicities estimated for GN 42912-NE and GN 42912-SW. We also explored the impact of choosing the density-bounded scenario case, and found marginal variations in the final estimates, within uncertainties. When applying this method to the 2796Å line, the intrinsic flux ratio of Mg IIλ2796/[O III]λ5008 from Xu et al. (2022) is expressed as follows:

$$R_{2796} = 0.074 \times \log(O_{32,\rm corr})^2 - 0.96 \times \log_{10}(O_{32,\rm corr}) - 0.49 \quad (5)$$

with $R_{2796} = \log(F_{\rm corr}({\rm Mg\,II}\lambda 2796)/F_{\rm corr}([{\rm O\,III}]\lambda 5008))$.

$O_{32,\rm corr}$ denotes the extinction-corrected O_{32} ratio. Using the dust-corrected emission line fluxes and O_{32} ratio, we calculate R_{2796} for both GN 42912-NE and GN 42912-SW, derive the intrinsic flux of the Mg II line, and juxtapose these with the measured Mg II line fluxes to deduce the relative escape fractions at 2796Å ($f_{\rm esc}^{\rm rel}$(2796)). Here, it is important to consider both the NDC and the βDC scenarios due to the use of extinction-corrected values for multiple lines.

For GN 42912-NE, we derive $f_{\rm esc}^{\rm rel}(2796) = 0.49 \pm 0.12$ in the NDC and 0.37 ± 0.10 in the βDC. For the NDC, this relative escape fraction directly translates to the LyC escape fraction. For the βDC, we convert the relative escape fraction into absolute $f_{\rm esc}^{\rm LyC}$ by multiplying them by the dust attenuation at 912Å, employing E(B-V) values extrapolated from β. We find $f_{\rm esc}^{\rm rel}(2796\rightarrow{\rm LyC})$ to be 0.063 ± 0.020 using the R16 dust extinction and 0.085 ± 0.023 using the SMC dust attenuation law. We note that these escape fraction are lower yet within 2σ of the values derived using the Doublet method for GN 42912-NE.

Applying the same approach to GN 42912-SW must be done carefully due to the lower limit on the O_{32} ratio, which is a quadratic term in Equation 5. However, for O_{32} ratios exceeding the lower limit reported for GN 42912-SW, the expression in 5 is dominated by the second-order polynomial degree term. Consequently, any ratio above this threshold would yield larger R_{2796}. Given that [O III] is detected and hence fixed, this implies that the inferred intrinsic Mg II flux derived using the lower limit of O_{32} is also a lower limit to the

Table 3. Mg II properties and Mg II-based LyC escape fractions for GN 42912-NE and GN 42912-SW. The Doublet Ratio method refers to the Chisholm et al. (2020) method for determining f_{esc}^{LyC} from the Mg II doublet and the Photoionization models method was originally introduced by Henry et al. (2018). We use two different scenarios, a dust free case (NDC) and β dust-case (βDC), where we use β as a tracer of E(B-V). The Mg II doublet is not detected in GN 42912-SW so only the Photoionization models method enable to derive upper limits on f_{esc}^{LyC}. The final estimates correspond to the realistic yet still conservative final estimates on f_{esc}^{LyC} for both galaxies after a careful discussion on the different scenarios considered in this work (see Section 5).

Property	GN 42912-NE		GN 42912-SW	
	NDC	βDC	NDC	βDC
Doublet Ratio method				
$R_{Mg\,II}$	1.19 ± 0.29		-	
N_{H_0}	$(8.9 \pm 5.4) \times 10^{16}$ cm^{-2}		-	
f_{esc}^{rel}(LyC)	0.57 ± 0.21		-	
f_{esc}^{abs}(LyC)	0.57 ± 0.21	0.12 ± 0.05 (R16) 0.16 ± 0.06 (SMC)	-	-
Photoionization models				
R_{2796}	-1.01 ± 0.08	-0.94 ± 0.09	> -1.16	> -1.05
f_{esc}^{rel}(2796)	0.489 ± 0.120	0.310 ± 0.079	< 0.469	< 0.24
f_{esc}^{abs}(2796 $\rightarrow$ LyC)	0.489 ± 0.120	0.063 ± 0.020 (R16) 0.085 ± 0.025 (SMC)	< 0.469	< 0.021 (R16) < 0.033 (SMC)
Final estimates				
f_{esc}^{abs}(LyC)	< 0.11		< 0.06	

actual intrinsic flux. As the observed Mg II flux is an upper limit, the resultant relative escape fractions derived using the respective flux limits unequivocally constitute upper limits to the true relative escape fraction. Our calculations yield $f_{esc}^{rel}(2796) < 47\%$ in the NDC and $< 24\%$ in the βDC. In the latter case, we can once again extrapolate $f_{esc}^{rel}(2796)$ at 912Å to estimate the ionizing escape fraction. The derived values reveal that $f_{esc}^{rel}(2796 \rightarrow LyC)$ is < 0.021 using the R16 dust extinction and < 0.033 using the SMC dust attenuation law.

In summary, the photoionization models approach indicates that both GN 42912-NE and GN 42912-SW have, in the most conservative case (no dust) f_{esc}^{LyC} below 50%. In a more realistic scenario where β traces the dust extinction, their final f_{esc}^{LyC} is relatively low, typically around 8% for GN 42912-NE and below 4% for GN 42912-SW. In this section, we have established multiple f_{esc}^{LyC} estimates to accommodate various scenarios and investigate the impact of dust, all of them being reported in Table 3. However, further discussion is warranted regarding the plausibility of these scenarios and the reliability of both the Doublet and photoionization methods. This will allow us to arrive at a single final estimate with greater confidence for GN 42912-NE and GN 42912-SW, facilitating comparison with cosmological models assessing the behavior of faint and massive galaxies during the EoR. This is the topic of the next section.

5 A PLAUSIBLE ABSENCE OF LYC ESCAPE IN TWO REIONIZATION-ERA GALAXIES

In the previous section, we explored diverse scenarios to estimate f_{esc}^{LyC} for both GN 42912-NE and GN 42912-SW, considering instances where both galaxies are either depleted of dust (NDC) or have dust extinction scaling with the measured β values for both objects (βDC). Across these scenarios, we observed a wide range of potential f_{esc}^{LyC} values, spanning from a few percent (βDC) to $\sim 50\%$ (NDC) for both objects. While this extensive range might initially appear to prevent definitive conclusions regarding the contribution of these galaxies during the EoR, this section highlights several key factors supporting that the LyC escape from these two objects is likely weak, if not absent.

In Section 5.1, we discuss surrounding the NDC and βDC assumptions. Section 5.2 examines our estimates in light of the caveats associated with Mg II-based indirect methods, as highlighted in Katz et al. (2022a).

5.1 The uncertainties on dust

In this study, we have carefully considered various scenarios to address uncertainties surrounding dust attenuation's impact on nebular lines or the shape of the dust extinction law. One such scenario posits that both galaxies are depleted of dust (NDC). Unsurprisingly, this scenario yields the highest estimates of LyC escape fractions, as the final escape fraction at 912Å relies solely on absorption from the neutral gas. However, the NDC scenario should be considered as an extreme and likely unrealistic case.

This is because, first, galaxies with $M_\star \sim 10^{8.5} M_\odot$ and 12+log(O/H)~8 seldom exhibit complete absence of dust extinction. While the super-early, relatively massive galaxies may be dust-free objects (e.g. Ziparo et al. 2023; Cullen et al. 2024), this primarily concerns to redshifts beyond 10. At $z \sim 7.5$, galaxies like GN 42912-NE and GN 42912-SW had time to form metals and dust aggregates.

Moreover, GN 42912-NE and GN 42912-SW have β slopes of -1.92 and -1.51, respectively. β slopes are intertwined with both the age of populations emitting the intrinsic stellar continuum and dust extinction. However, Chisholm et al. (2022) demonstrated that for galaxies dominated by young stellar populations, the stellar continuum slope minimally affects β, which predominantly correlates with dust extinction levels in galaxies. The β slopes of GN 42912-NE and GN 42912-SW imply respective E(B-V) values of approximately ~0.134 (~0.043) and 0.204 (0.066), under the R16 (SMC) dust extinction law. The remarkably tight β-to-E(B-V) correlation at low redshift makes the βDC scenario more plausible than the NDC. The latter should therefore be viewed as an extreme and highly conservative scenario.

In this study, we also separately evaluated f_{esc}^{LyC} estimates based on the R16 dust extinction laws (Reddy et al. 2016) and based on the SMC extinction law (Gordon et al. 2003). Due to significant differences in their shapes, this approach offers valuable insights into how the form of dust extinction, which remains largely uncertain for galaxies at $z > 6$, influences f_{esc}^{LyC} values. The variations in final f_{esc}^{LyC} estimates when considering either law are relatively minor (e.g., 0.063 ± 0.020 versus 0.085 ± 0.025 for GN 42912-

NE) and falling within 1σ uncertainties. As the attenuation at 912Å (A(912Å)=(E(B–V)*k(912Å)) is higher for the R16 law, the f_{esc}^{LyC} estimates derived using the SMC law are always larger than when using the R16 law. Since most high redshift galaxies studies use SMC dust extinction laws, we opt to consider only values derived using the SMC law hereafter. Yet we note that opting for the R16 estimates would not impact the conclusions of this work.

5.2 The caveat of Mg II based approaches

Predicting LyC escape fractions indirectly is complex, as most of the best LyC diagnostics found at low redshifts come with certain caveats. This is true for Mg II-based approaches as well. Fortunately, Katz et al. (2022b) investigated a comprehensive list of caveats associated with these approaches, providing us the necessary tools to understand and test the reliability of our approach. In the following subsections, we discuss the limitations of the Doublet ratio method and then delve into the caveats of the photoionization models we utilized.

5.2.1 Caveats of the Mg II doublet method

One significant caveat of the Mg II doublet method is that it relies on the optically thin regime for accurate f_{esc}^{LyC} estimates. This means that the method is most reliable when the doublet ratio is close to 2. However, as we venture further into the optically thin regime, resonant radiative transfer effects become increasingly significant. These effects alter the shape of the doublet lines and tend to bring the doublet ratios closer to 1.

This phenomenon implies that as the observed doublet ratio (Mg II) decreases, there is a risk of significantly overpredicting the f_{esc}^{LyC} derived using the doublet method. This effect is somewhat observed in the analysis of Katz et al. (2022a), whose authors conducted tests on the reliability of this approach using galaxies from the SPHINX cosmological simulation suite. For example, Figure 17 shows that that predictions based on R(Mg II) substantially overestimate the true escape fraction, and this overestimation is more and more substantial for decreasing f_{esc}^{LyC}. In their simulations, f_{esc}^{LyC} is primarily influenced by neutral gas, with dust playing a minor role in removing ionizing photons. Consequently, lower f_{esc}^{LyC} values are likely consistent with the presence of denser neutral gas environments where the Mg II ratio deviates from the optically thin regime.

In our analysis, we find a doublet ratio of 1.19 for GN 42912-NE, suggesting that we are already far from the optically thin regime for this galaxy. Therefore, our f_{esc}^{abs} estimates based on the Doublet ratio may significantly overpredict the true LyC escape and should be strictly regarded as upper limits.

5.2.2 Caveats of the photoionisation-based method

The photoionization-based method is less sensitive to the assumption of the optically thin regime because it hinges on determining the intrinsic Mg II flux from other observables. This method relies on CLOUDY models to deduce the intrinsic Mg II luminosity based on optical lines from O II and O III. Initially proposed by Henry et al. (2018) using idealized CLOUDY models, this approach was later refined and extended by Xu et al. (2022). In our study, we utilized the Mg II to O_{32} relation from the latter work to estimate the intrinsic flux for GN 42912-NE and GN 42912-SW.

However, as highlighted by Katz et al. (2022b), this method is not without caveats. In their analysis using galaxies from the SPHINX cosmological suite, the authors observed that while the Mg II to O_{32} relation proposed by Henry et al. (2018) generally matches the simulated galaxies reasonably well, there is a notable scatter, with most SPHINX galaxies tending to lie above the relation. Consequently, predictions based on the Henry et al. (2018) relation could underestimate the true escape fraction by -0.2 to -1 dex (see their Figure 15). Given that the relations from Xu et al. (2022) are derived using a similar methodology, it is plausible that they may suffer from similar biases.

Therefore, while the photoionization-based method may offer an alternative to the doublet ratio approach, we must carefully consider to potential biases inherent in the underlying relations. Indeed, an underprediction of the intrinsic flux implies that we likely overestimated the relative (and consequently, absolute) escape fraction of LyC photons using this method. Katz et al. (2022b) proposed updated relations (their equation (4)) to derive a more accurate Mg II intrinsic luminosity based on O II and O III lines. Using their equation in the βDC, we a relative escape fraction of ionizing photons of 8.5% for GN 42912-NE, as compared to 31% where using the Xu et al. (2022) equation. This means here that the f_{esc}^{LyC} estimates obtained using the photoionization-based method should also be treated as strict upper limts.

Thus far, our analysis has highlighted several key points: (1) the NDC values are likely too extreme to be relevant, (2) the f_{esc}^{LyC} estimates from the Doublet method are least reliable for GN 42912-NE due to the non-validity of the optically thin regime, and (3) while the f_{esc}^{LyC} derived from photoionization models are likely more reliable, they also tend to underpredict the intrinsic Mg II flux, suggesting that the estimated f_{esc}^{LyC} should be considered as upper limits. Considering these aspects collectively, we determine the derived f_{esc}^{LyC} from the photoionization-based method, utilizing the SMC dust extinction law, as final realistic upper limits for both GN 42912-NE and GN 42912-SW.

Rather than directly taking the central values as upper limits, we utilize the central values $+1\sigma$. Thus, the final f_{esc}^{LyC} estimates for GN 42912-NE are < 0.11 (0.085+0.025), and < 0.058 (0.033+0.025) for GN 42912-SW. These values are reported in Table 3 and are used hereafter to assess the contributions of GN 42912-NE and GN 42912-SW in the context of low-z observations and reionization models.

6 COMPARISON WITH LOW-Z MG II CONSTRAINTS

In the previous section, we demonstrated that while indirect methods utilizing Mg II suffer from certain limitations, these caveats imply that we have likely consistently overestimated the expected f_{esc}^{LyC} using the methods outlined in Section 4. Consequently, by meticulously considering these issues, we can infer that the true escape fractions are likely weak and less than approximately 11% and 6% for GN 42912-NE and GN 42912-SW, respectively.

Here, we delve into how these estimates compare to observations of LyC leaking galaxies at low redshifts. In Section 6.1, we compare the Mg II profile of GN 42912-NE with those of a similar low-redshift leaking galaxy, while Section 6.2 places our f_{esc}^{LyC} estimates in context with trends observed in low-redshift samples.

6.1 Comparison to low-z Mg II profiles

For two decades or more, the observations of LyC leaking galaxies remained scarce (Leitet et al. 2013; Leitherer et al. 2016; Borthakur et al. 2014; Izotov et al. 2016b,a, 2018a,b). A significant breakthrough occurred with the LzLCS program (PI: Jaskot) (Flury et al.

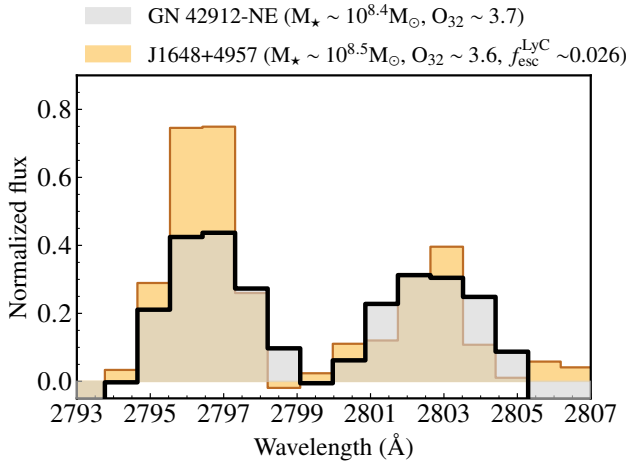

Figure 3. Comparison of the Mg II profile of GN 42912-NE (in black) with that of a low-z LyC leaker, J1648+4957 (in orange), from the LzLCS sample (Flury et al. 2022a). J1648+4957 exhibits similar properties to GN 42912-NE and has a weak escape fraction (< 3%). The profile of J1648+4957, taken from Leclercq et al. (2024), has been adjusted to the resolution of JWST-G235H. In J1648+4957, R(Mg II) is 1.98, indicative of a relative escape fraction of 100%, with dust being the primary absorber of ionizing photons. In contrast, R(Mg II) for GN 42912-NE is 1.22, suggesting a denser neutral gas environment.

2022a), which quadrupled the number of detected LyC leaking galaxies at $z < 1$, providing a unique sample to derive indirect diagnostics relevant for high redshifts (Flury et al. 2022b) and understand the physical mechanisms underlying the escape of ionizing photons (e.g., Saldana-Lopez et al. 2022; Amorín et al. 2024; Leclercq et al. 2024).

Xu et al. (2023) and Leclercq et al. (2024) presented the Mg II emission profiles of LyC leaking galaxies from the LzLCS sample. Their profiles highlight a striking conclusion: most of the LyC leaking galaxies with detected leakage have Mg II emission profiles with R(Mg II)~2, suggesting they are in the optically thin regime and the neutral hydrogen gas does not significantly absorb the escaping ionizing photons. In Figure 3, we compare the Mg II profile of GN 42912-NE with the profile of one low-redshift leaker from the LzLCS, J1648+4957, a galaxy with similar properties as GN 42912-NE with $M_\star \sim 10^{8.5}$ $M_\odot$ and $O_{32} \sim 3.6$, and with a relatively weak $f_{esc}^{LyC} = 0.026^{+0.051}_{-0.014}$. The f_{esc}^{LyC} of this object is determined using a direct method, i.e., comparing direct observations of the flux at 912Å with UV SED continuum models (Flury et al. 2022a).

Figure 3 highlights that J1648+4957 has its 2796Å line much stronger than its 2803Å line, and we derived a Mg II doublet ratio of ~1.96. The relative escape fractions derived from the doublet ratio are close to 100%, indicating that neutral gas plays a minor role in regulating the LyC escape. Rather, its f_{esc}^{LyC} is largely driven by dust extinction, which removes ~97% of the escaping radiation in J1648+4957 (E(B-V)(R16) is 0.1636, Leclercq et al. 2024). It is clear from Figure 3 that the Mg II profile of GN 42912-NE differs notably from that of J1648+4957. As discussed earlier, the Mg II profile of GN 42912-NE suggests an overall relatively dense neutral gas environment, which acts as the major sink for ionizing photons. This observation further strengthens the notion that the f_{esc}^{LyC} in GN 42912-NE is likely weak, and possibly even absent.

It is important to note that comparing higher-redshift objects to lower-redshift analogues comes with caveats. The first few years of JWST observations have revealed a population of high-redshift objects with significantly different properties than those found in the local universe. It's possible that in the higher-redshift universe, galaxies harbor much larger amounts of neutral gas compared to what is observed in the low-redshift universe. Consequently, the typical escape fraction of high-redshift galaxies may be significantly smaller than what is observed at lower redshifts. This potential difference may prove to be a critical aspect, especially in light of the current ionizing photon budget crisis. Pre-JWST reionization models, primarily built upon low-redshift observations, face a significant challenge when reconciling their predictions with the current JWST constraints on the emissivity of reionization-era galaxies (Muñoz et al. 2024). This discrepancy suggests that there may be fundamental differences in the expected properties of reionization galaxies, and one of these difference may be that high-z objects have substantially lower f_{esc}^{LyC} than assumed before JWST. We discuss this point in Section 7.

6.2 Comparison to low-z trends

Here, we compare the upper limits on f_{esc}^{LyC} for GN 42912-NE and GN 42912-SW with LyC trends observed within the low-z universe. Notably, Flury et al. (2022b), building upon a sample of ~ 60 galaxies spanning non-leakers, weak leakers, and strong leakers, unveiled significant correlations between f_{esc}^{LyC} and various properties such as Lyα profiles, O_{32}, β, and the surface density of star formation (ΣSFR). Here we focus only on the relation of f_{esc}^{LyC} to three properties: the β slopes at 1500Å, the O_{32} ratios, and $W_\lambda(H\beta)$. We note that GN 42912 was initially detected by Finkelstein et al. (2013) due to relatively robust Lyα emission (W_λ ~33 ± 3, see Jung et al. 2020). Yet, PRISM observations from JADES (cite here) show an absence of Lyα emission for the same system. This is likely due to a sub-optimal slit positioning in the context of JADES which only partially encompasses both sources, likely capturing only the regions devoid of Lyα emission. Consequently, because the Lyα properties of GN 42912-NE and GN 42912-SW are intricate and presumably not spatially homogeneous, we opt to refrain from incorporating the Lyα properties of the entire GN 42912 system into this comparison.

Figure 4 shows three panels illustrating the comparison of f_{esc}^{LyC} with β, O32, and $W\lambda(H\beta)$. We observe that the upper limits derived for GN 42912-NE and GN 42912-SW consistently align with the f_{esc}^{LyC} to β and O_{32} trends. Regarding the f_{esc}^{LyC} to $W\lambda(H\beta)$ comparison, the upper limits slightly exceed the primary trends but remain consistent, considering their nature as upper limits.

In summary, Figure 4 highlights that the f_{esc}^{LyC} upper limits determined for GN 42912-NE and GN 42912-SW are likely realistic within the context of trends observed in the low-z universe. However, the validity of this comparison hinges on the extent to which higher redshift objects can be appropriately compared with their low-redshift counterparts. Ultimately, only future observations and constraints on the f_{esc}^{LyC} of high-z galaxies will bring clarity on this matter.

In the next section, we discuss the implications of our limits within the context of cosmological models predicting the influence of star-forming galaxies during reionization.

7 LIMITED CONTRIBUTION FOR RELATIVELY BRIGHT GALAXIES DURING REIONIZATION ?

Here we discuss the f_{esc}^{LyC} constraints on GN 42912-NE and GN 42912-SW with respect to cosmological reionization models

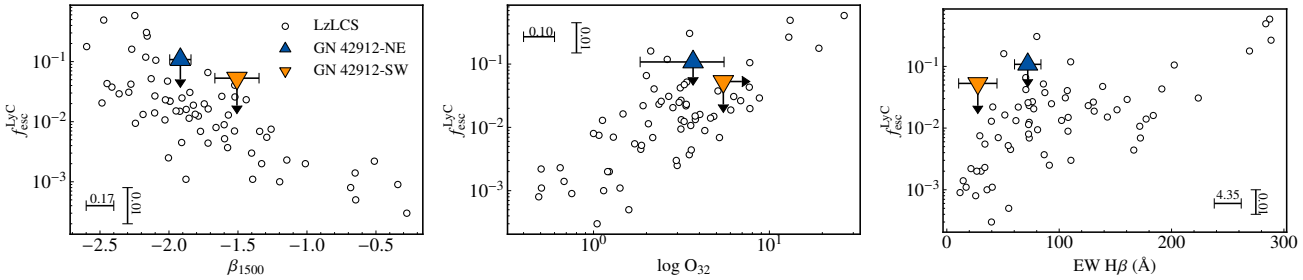

Figure 4. Comparison of the upper limits on f_{esc}^{LyC} for GN 42912-NE (blue) and GN 42912-SW (orange) with LyC trends observed within the low-z universe using the LzLCS sample (Flury et al. 2022a), which encompasses a range of $z < 0.5$ galaxies including non-leakers, weak leakers, and strong leakers. The trends are depicted with respect to β slopes (left), O32 ratios (middle), and $W\lambda(H\beta)$ (right). Each panel includes typical uncertainties on the LzLCS data points, represented by non-scaled horizontal and vertical error bars placed in one corner. Overall, the upper limits on f_{esc}^{LyC} for GN 42912-NE and GN 42912-SW consistently align with the observed trends.

(Section 7.1) and in the context of the current JWST ionizing budget crisis (Section 7.2).

7.1 Bright galaxies versus faint galaxies

In theory, understanding the drivers of reionization is relatively straightforward: we need to identify the astronomical objects that contribute the most to the ionizing photon budget and enable the ionization of neutral hydrogen by $z \sim 6$. Pre-JWST studies have predominantly indicated that star-forming galaxies, rather than AGNs, played a dominant role in reionization (e.g., Robertson et al. 2015; Finkelstein et al. 2019). Two primary models have emerged from these studies: one model is characterized by relatively faint objects (MUV > -15) with escape fractions between ~ 5 and 10% during reionization (Finkelstein et al. 2019), while the other model is dominated by brighter galaxies (MUV < -19) exhibiting a higher average escape fraction of ionizing photons, $f_{esc}^{LyC} \sim 5$ to 20% during the EoR (Naidu et al. 2022; Matthee et al. 2022). Notably, in the latter model, the average escape fraction is derived from the Lyα luminosity function, assuming that 50% of bright LAEs (L$> 10^{42.2}$ erg s^{-1}) leak 50% of the ionizing photons they produce. While both are distinct models to explain reionization, they both yield predictions that are consistent with current constraints on the reionization history as well as yield correct values for τ_{CMB}.

In this section, we compare our f_{esc}^{LyC} estimates for GN 42912-NE and GN 42912-SW within the framework of these models. We note that current JWST observations are not consistent with either model, but we delve into this aspect in the next section. In Figure 5, we present two observationally-based cosmological models that describe the evolution of the average f_{esc}^{LyC} as a function of UV magnitude, taken at 1500Å. The model proposed by Matthee et al. (2022), mentioned earlier, is grounded in the observations of bright LAEs with anticipated LyC escape fraction of $\sim$ 50% (Naidu et al. 2022). Utilizing these observations alongside the Lyα luminosity function and the assumption that 50% of these LAEs exhibit such a high f_{esc}^{LyC}, the authors conducted simulations to infer the evolution of f_{esc}^{LyC} as a function of M1500, which rises with redshift and peaks at an average f_{esc}^{LyC} of 0.15 for M1500 ~ -20 around $z \sim 6.59$. This model posits that relatively bright galaxies dominate the ionizing photon budget.

In contrast, Chisholm et al. (2022) developed a model dominated by faint galaxies using the LzLCS sample (Flury et al. 2022a). This model is based on a tight β to f_{esc}^{LyC} relation and the evolution of the

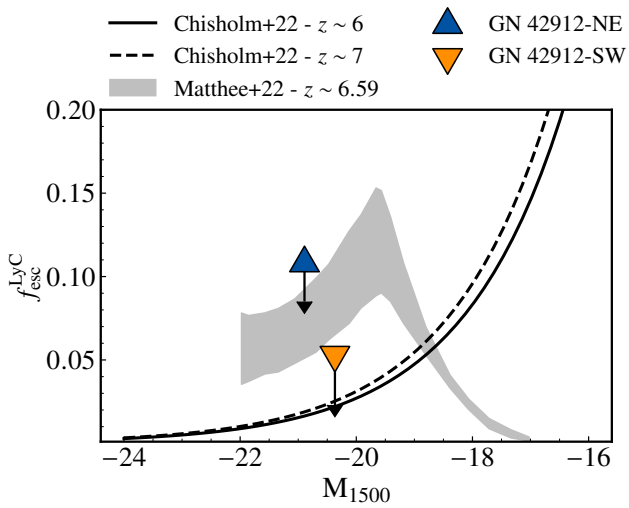

Figure 5. The evolution of f_{esc}^{LyC} around $z = 7$ as a function of UV magnitude within the context of two cosmological models and the f_{esc}^{LyC} constraints established in this work. The model proposed by Matthee et al. (2022), based on observations of bright LAEs exhibiting $f_{esc}^{LyC} \sim$ 50% at $z \sim 3$ (Naidu et al. 2022), suggests a dominant contribution from relatively more massive and luminous objects to the ionizing budget. In contrast, the model proposed by Chisholm et al. (2022), relying on the β-to-f_{esc}^{LyC} relation identified in the LzLCS sample and leveraging the β–MUV relation established by Bouwens et al. (2014), argues for the dominance of relatively faint galaxies at high-z. While the f_{esc}^{LyC} constraints for GN 42912-NE and GN 42912-SW do not definitively favor either model, they do not align entirely with models suggesting that bright galaxies could potentially leak approximately 50% of the intrinsically produced ionizing photons.

β–MUV Color–Luminosity Relationship established by Bouwens et al. (2014). This relation is redshift-dependent, suggesting that at $z > 6$, galaxies with MUV > -19 should primarily contribute to the ionizing photon budget by allowing a large number of ionizing photons to escape. Figure 5 illustrates how these two models behave in opposite directions, particularly evident in the presence of a cross-turnover around $M_{UV} \sim -19$, where brighter objects dominate in the Matthee et al. (2022) model and fainter objects dominate in the Chisholm et al. (2022) model.

We have overlaid the constraints on GN 42912-NE and GN 42912-SW on this figure. As conservative upper limits, Figure 5 demon-

strates that these constraints alone do not offer conclusive evidence for favoring one model over the other. However, the Matthee et al. (2022) model is built on the assumption that 50% of bright LAEs exhibit $f_{esc}^{LyC} \sim 50\%$. Since f_{esc}^{LyC} is $< 11\%$ for GN 42912-NE and $< 6\%$ for GN 42912-SW, we can safely assume that these two galaxies have not significantly contributed to reionization as bright LAEs leakers would in the Matthee et al. (2022) model. Yet, our conclusion rely solely on two objects such that it is imperative to establish additional, and ideally more precise, constraints on the f_{esc}^{LyC} of high-z galaxies to effectively constrain the prevalence of a certain bright or faint galaxy model.

7.2 Current f_{esc}^{LyC} constraints in the context of JWST photon budget crisis

The previous section primarily focused on comparing the constraints on f_{esc}^{LyC} of two $M_{UV} \sim -20.5$ galaxies at $z \sim 7.5$ within the context of pre-JWST models, somewhat overlooking recent findings that introduce new uncertainties to these established models. Recent JWST observations have unveiled early galaxies with notably high ionizing efficiencies ($\log \eta_{ion} \geq 25.5$ Atek et al. 2024; Simmonds et al. 2024; Endsley et al. 2023a; Prieto-Lyon et al. 2023; Hsiao et al. 2024), while also revealing highly star-forming galaxy populations at $z > 9$ (Finkelstein et al. 2023; Harikane et al. 2023; Mason et al. 2023; Eisenstein et al. 2023). These observations introduce a discrepancy in current reionization models. Muñoz et al. (2024) shows that the exceedingly high ionizing efficiencies and the presence of early-type relatively massive and star-forming galaxies challenge theoretical ionizing budgets, suggesting an extremely rapid reionization concluding at $z > 8.5$, which conflicts with τ_{CMB} measurements from Planck (Planck Collaboration et al. 2021).

Muñoz et al. (2024) explores potential solutions to resolve this ionizing photon budget crisis. One proposed explanation is that f_{esc}^{LyC} is considerably lower than expected based on models derived from lower redshift observations, such as those discussed in the previous section from Matthee et al. (2022) and Chisholm et al. (2022). This scenario becomes feasible if high-redshift galaxies harbor larger and denser neutral gas environments, substantially reducing the final f_{esc}^{LyC} and their overall contribution to reionization.

Our current constraints on f_{esc}^{LyC} offer limited yet interesting insights in the context of this ionizing budget crisis. While the upper limits derived in this study do not conflict with pre-JWST reionization models, the Mg II doublet within GN 42912-NE strongly suggests a dense neutral gas environment, indicating that the relative escape fraction (i.e., the escape fraction solely dictated by the neutral gas without considering potential dust) must be lower than 57%. As highlighted earlier, this relative escape fraction significantly diverges from observations of low-z leakers with similar galaxy properties, which exhibit R(Mg II~2) and therefore a relative LyC escape fraction near 100% (as discussed in Section6.1, dust is the dominant absorber of ionizing photons in this galaxies, see also Chisholm et al. 2022). Thus, the Mg II doublet of GN 42912-NE suggests the presence of significantly higher hydrogen gas density, which could potentially lower the overall f_{esc}^{LyC} of reionization-era galaxy populations (when considering the combined attenuation of neutral gas plus dust) if such scenarios are prevalent.

Further insights and constraints may emerge by considering the entire sample of 10 galaxies within JWST program ID 1861, which also have Mg II coverage. This represents the next phase of our work. Additional constraints on the f_{esc}^{LyC} of galaxies at $z > 6$ are crucial to understanding potential solutions to the current ionizing budget crisis. Ideally, constraints that combine multiple LyC tracers such as Mg II but also Lyα (Verhamme et al. 2015, 2017; Izotov et al. 2020; Gazagnes et al. 2020; Choustikov et al. 2024) would offer more robust insights and tighter constraints on f_{esc}^{LyC}.

I measure ϵ of 24 for GN 42912-NE ????? Can we check this.

8 CONCLUSIONS

In this study, we analyzed the JWST NIRSpec high-resolution G235H and G395H observations of GN 42912, a bright Lyα system at $z \sim 7.5$ initially reported by Finkelstein et al. (2013). These observations were part of the JWST program 1871 (PI: Chisholm), with the primary objective of detecting the Mg II$\lambda\lambda$2796,2803 doublet to indirectly estimate the escape fraction of ionizing photons, building upon methodologies established and calibrated in the low-z universe by Henry et al. (2018) and Chisholm et al. (2020).

The JWST observations unveiled that GN 42912 comprises two galaxies, denoted as GN 42912-NE and GN 42912-SW, separated by ~125Mpc and an angular distance of 0.1″. GN 42912-NE has a stellar mass of $\sim 10^{8.4}$M$\odot$, a UV magnitude of -20.37 mag, $\beta \sim -1.92$, a moderate O32 ratio of 3.7, and a gas-phase metallicity estimated at $\sim$ 8.05 using the R_{23} method. Meanwhile, GN 42912-SW features a stellar mass of $\sim 10^{8.9}$M$\odot$, a UV magnitude of -20.89 mag, $\beta \sim -1.51$, an O32 ratio exceeding 5.47, and a gas-phase metallicity estimated around $\sim$ 8.09 using the R_{23} method.

Our analysis primarily focused on the Mg II$\lambda\lambda$2796, 2803 observations of both GN 42912-NE and GN 42912-SW to constrain the escape of ionizing photons from these objects. GN 42912-NE exhibits clear $> 3\sigma$ detections of both lines, enabling us to employ two distinct approaches, the Mg II doublet approach relying on the ratio of the two lines (Chisholm et al. 2020), and comparison to the Mg II intrinsic flux determined using photoionization models (Henry et al. 2018). The Mg II doublet is not detected in GN 42912-SW, but we use the derived upper limits to extract an upper limit on f_{esc}^{LyC}.

We calculated several estimates of the LyC escape fraction considering multiple scenarios, including scenarios with and without dust attenuation. We also explored the impact of dust attenuation by employing two different dust extinction laws: the SMC law (Gordon et al. 2003) and the Reddy et al. (2016) attenuation law.

In our analysis, we find that considering different scenarios yields a broad range of estimates for f_{esc}^{LyC}, from negligible leakage (around $\sim 5\%$) in the presence of dust to $\sim 50\%$ of ionizing photons escaping in the absence of dust. However, in Section 5, we argue that the no-dust scenario is an extreme case unlikely to accurately represent the true conditions in GN 42912-NE and GN 42912-SW. We also address important caveats associated with the Mg II indirection approaches used to estimate f_{esc}^{LyC}, which in our cases suggest that our estimates overpredict the escape of ionizing photons and should be regarded as strict upper limits. We conclude that f_{esc}^{LyC} is realistically less than 11% in GN 42912-NE and less than 6% in GN 42912-SW.

In Section 6, we compared these estimates to trends established from LyC leakers in the $z < 0.5$ universe (Flury et al. 2022a), demonstrating that they align consistently with the f_{esc}^{LyC}-β, f_{esc}^{LyC}-O32, and f_{esc}^{LyC}-Wλ(Hβ) relations. Furthermore, we highlighted that the Mg II profiles of GN 42912-NE significantly differ from those of low-z leakers, where the ratio of both lines is consistently close to 2. This divergence suggests that GN 42912-NE is dominated by a dense neutral hydrogen environment that removes a significant amount of LyC

photons, a scenario distinct from low-z leakers where dust serves as the primary sink of ionizing radiation.

Finally, 7 discusses these first constraints in the context of cosmological reionization models, namely one model where relatively faint galaxies ($M_{UV} > -19$) dominate reionization (Finkelstein et al. 2019; Chisholm et al. 2022), and one model where brighter objects furnishes the bulk of ionizing photons ($M_{UV} > -19$) (Matthee et al. 2022). We show that the current constraints give limited constraints on the preference of one or the other model, but seems incompatible with scenarios where the universe is dominated by a few bright objects have large f_{esc}^{LyC} ($\sim 50\%$). Finally, we also consider our constraints in the context of the current JWST ionizing budget crisis (Muñoz et al. 2024). The Mg II profile of GN 42912-NE, hinting at large amount of hydrogen gas absorbing the escape radiation, may be consistent with new cosmological models which solve the tension by significantly decreasing the average f_{esc}^{LyC} of the contribution galaxies to $\sim 3\%$, where this decrease being due to an overdensity of hydrogen within galaxies efficiently absorbing the LyC photons.

This paper sets the first Mg II-based constraints on f_{esc}^{LyC} of galaxies within the Epoch of Reionization. Although these constraints are not enough to determine the preferential cosmological reionization models, they set a first step in that direction by showing a weak, possibly null leakage from two relatively bright $z \sim 7.5$ galaxies. More constraints will be needed to improve our understanding of the contribution of faint and bright star-forming galaxies during reionization.

ACKNOWLEDGEMENTS

SG is grateful for the support enabled by the Harlan J. Smith McDonald fellowship which made this project possible.

DATA AVAILABILITY

The data underlying this paper is available upon reasonable request.

REFERENCES

Amorín R. O., et al., 2024, A&A, 682, L25
Asplund M., Amarsi A. M., Grevesse N., 2021, A&A, 653, A141
Atek H., et al., 2024, Nature, 626, 975
Bait O., et al., 2023, arXiv e-prints, p. arXiv:2310.18817
Barbary K., 2016, The Journal of Open Source Software, 1, 58
Bian F., Fan X., McGreer I., Cai Z., Jiang L., 2017, The Astrophysical Journal, 837, L12
Böker T., et al., 2023, PASP, 135
Borthakur S., Heckman T. M., Leitherer C., Overzier R. A., 2014, Science, 346, 216
Bouwens R. J., et al., 2014, ApJ, 793, 115
Bouwens R. J., et al., 2015, ApJ, 803, 34
Boyer M. L., et al., 2022, Research Notes of the American Astronomical Society, 6, 191
Brammer G., 2019, Grizli: Grism redshift and line analysis software, Astrophysics Source Code Library, record ascl:1905.001 (ascl:1905.001)
Brammer G., 2023, msaexp: NIRSpec analyis tools, Zenodo, doi:10.5281/zenodo.7299500
Bruzual G., Charlot S., 2003, MNRAS, 344, 1000
Cameron A. J., Katz H., Witten C., Saxena A., Laporte N., Bunker A. J., 2023, Nebular dominated galaxies in the early Universe with top-heavy stellar initial mass functions (arXiv:2311.02051)
Carnall A. C., McLure R. J., Dunlop J. S., Davé R., 2018, MNRAS, 480, 4379
Chisholm J., Prochaska J. X., Schaerer D., Gazagnes S., Henry A., 2020, MNRAS, 498, 2554
Chisholm J., et al., 2022, MNRAS, 517, 5104
Choustikov N., et al., 2024, arXiv e-prints, p. arXiv:2401.09557
Cullen F., et al., 2024, MNRAS,
Curti M., Mannucci F., Cresci G., Maiolino R., 2020, MNRAS, 491, 944
Donnan C. T., et al., 2023, MNRAS, 518, 6011
Eisenstein D. J., et al., 2023, arXiv e-prints, p. arXiv:2306.02465
Endsley R., Stark D. P., Whitler L., Topping M. W., Chen Z., Plat A., Chisholm J., Charlot S., 2023a, MNRAS, 524, 2312
Endsley R., Stark D. P., Whitler L., Topping M. W., Chen Z., Plat A., Chisholm J., Charlot S., 2023b, MNRAS, 524, 2312
Ferland G. J., et al., 2017, Rev. Mex. Astron. Astrofis., 53, 385
Ferrara A., Pallottini A., Dayal P., 2023, MNRAS, 522, 3986
Finkelstein S. L., et al., 2013, Nature, 502, 524
Finkelstein S. L., et al., 2015, ApJ, 810, 71
Finkelstein S. L., et al., 2019, ApJ, 879, 36
Finkelstein S. L., et al., 2023, ApJ, 946, L13
Fletcher T. J., Tang M., Robertson B. E., Nakajima K., Ellis R. S., Stark D. P., Inoue A., 2019, ApJ, 878, 87
Flury S. R., et al., 2022a, ApJS, 260, 1
Flury S. R., et al., 2022b, ApJ, 930, 126
Gazagnes S., Chisholm J., Schaerer D., Verhamme A., Izotov Y., 2020, A&A, 639, A85
Gordon K. D., Clayton G. C., Misselt K. A., Landolt A. U., Wolff M. J., 2003, ApJ, 594, 279
Guseva N. G., Izotov Y. I., Fricke K. J., Henkel C., 2019, A&A, 624, A21
Harikane Y., et al., 2023, ApJS, 265, 5
Henry A., Berg D. A., Scarlata C., Verhamme A., Erb D., 2018, ApJ, 855, 96
Hsiao T. Y.-Y., et al., 2024, arXiv e-prints, p. arXiv:2404.16200
Hutchison T. A., et al., 2019, ApJ, 879, 70
Izotov Y. I., Schaerer D., Thuan T. X., Worseck G., Guseva N. G., Orlitová I., Verhamme A., 2016a, MNRAS, 461, 3683
Izotov Y. I., Orlitová I., Schaerer D., Thuan T. X., Verhamme A., Guseva N. G., Worseck G., 2016b, Nature, 529, 178
Izotov Y. I., Schaerer D., Worseck G., Guseva N. G., Thuan T. X., Verhamme A., Orlitová I., Fricke K. J., 2018a, MNRAS, 474, 4514
Izotov Y. I., Worseck G., Schaerer D., Guseva N. G., Thuan T. X., Fricke A. V., Orlitová I., 2018b, MNRAS, 478, 4851
Izotov Y. I., Schaerer D., Worseck G., Verhamme A., Guseva N. G., Thuan T. X., Orlitová I., Fricke K. J., 2020, MNRAS, 491, 468
Jenkins E. B., 2009, ApJ, 700, 1299
Jung I., et al., 2020, ApJ, 904, 144
Katz H., et al., 2022a, arXiv e-prints, p. arXiv:2211.04626
Katz H., et al., 2022b, MNRAS, 515, 4265
Kramida A., Ralchenko Y., Reader J., Team N. A., 2022, NIST Atomic Spectra Database (version 5.10), Online, doi:10.18434/T4W30F, https://physics.nist.gov/asd
Kroupa P., Boily C. M., 2002, MNRAS, 336, 1188
Labbé I., et al., 2023, Nature, 616, 266
Lebigot E. O., 2023, Uncertainties: a Python package for calculations with uncertainties, Online, http://pythonhosted.org/uncertainties/
Leclercq F., et al., 2024, arXiv e-prints, p. arXiv:2401.14981
Leitet E., Bergvall N., Hayes M., Linné S., Zackrisson E., 2013, A&A, 553, A106
Leitherer C., Hernandez S., Lee J. C., Oey M. S., 2016, ApJ, 823, 64
Mason C. A., Trenti M., Treu T., 2023, MNRAS, 521, 497
Matthee J., et al., 2022, Monthly Notices of the Royal Astronomical Society, 512, 5960
McElwain M. W., et al., 2023, PASP, 135, 058001
Muñoz J. B., Mirocha J., Chisholm J., Furlanetto S. R., Mason C., 2024, arXiv e-prints, p. arXiv:2404.07250
Naidu R. P., Tacchella S., Mason C. A., Bose S., Oesch P. A., Conroy C., 2020, ApJ, 892, 109
Naidu R. P., et al., 2022, MNRAS, 510, 4582
Oesch P. A., et al., 2023, MNRAS, 525, 2864

Ouchi M., et al., 2009, ApJ, 706, 1136
Planck Collaboration et al., 2016, A&A, 596, A108
Planck Collaboration et al., 2021, A&A, 652, C4
Prieto-Lyon G., et al., 2023, ApJ, 956, 136
Reddy N. A., Steidel C. C., Pettini M., Bogosavljević M., 2016, ApJ, 828, 107
Rigby J., et al., 2023, PASP, 135, 048001
Rivera-Thorsen T. E., Östlin G., Hayes M., Puschnig J., 2017, ApJ, 837, 29
Robertson B. E., Ellis R. S., Furlanetto S. R., Dunlop J. S., 2015, ApJ, 802, L19
Saldana-Lopez A., et al., 2022, A&A, 663, A59
Scarlata C., Hayes M., Panagia N., Mehta V., Haardt F., Bagley M., 2024, On the universal validity of Case B recombination theory (arXiv:2404.09015)
Shapley A. E., Steidel C. C., Strom A. L., Bogosavljević M., Reddy N. A., Siana B., Mostardi R. E., Rudie G. C., 2016, ApJ, 826, L24
Simmonds C., et al., 2024, MNRAS, 527, 6139
Steidel C. C., Bogosavljević M., Shapley A. E., Reddy N. A., Rudie G. C., Pettini M., Trainor R. F., Strom A. L., 2018, ApJ, 869, 123
Topping M. W., et al., 2024, Metal-poor star formation at $z > 6$ with JWST: new insight into hard radiation fields and nitrogen enrichment on 20 pc scales (arXiv:2401.08764)
Vanzella E., et al., 2015, A&A, 576, A116
Verhamme A., Orlitová I., Schaerer D., Hayes M., 2015, A&A, 578, A7
Verhamme A., Orlitová I., Schaerer D., Izotov Y., Worseck G., Thuan T. X., Guseva N., 2017, A&A, 597, A13
Worseck G., et al., 2014, MNRAS, 445, 1745
Xu X., et al., 2022, ApJ, 933, 202
Xu X., et al., 2023, ApJ, 943, 94
Yanagisawa H., et al., 2024, Balmer Decrement Anomalies in Galaxies at z 6 Found by JWST Observations: Density-Bounded Nebulae or Excited H I Clouds? (arXiv:2403.20118)
Ziparo F., Ferrara A., Sommovigo L., Kohandel M., 2023, MNRAS, 520, 2445
de Barros S., et al., 2016, A&A, 585, A51

APPENDIX A: CLEANING GN 42912 OBSERVATIONS

Here we briefly detail the methodology used to perform the background subtraction of the G235H and G395H data. As mentioned in 2, given the peculiar structure of the entire system composed of the two close-by galaxies, the 2D observations deserved a slightly more careful approach for their reduction, in particular regarding bright emission lines which are sufficiently compact so that the nodding approach for estimating the background works well.

In A1, we show the typical default subtraction using MSAEXP which build upon the nodding strategy i.e., observations with the telescope is inclined by a slight degree are used so that the background can be estimated from the slits where the central sources are shifted. The right panel shows that such default subtraction leaves two significant "holes" in the 2-D data set, where the flux per pixel is negative. Note that in most case where the central 2-D emission clumps are relatively compact, such strategy works well because one can extract the final 1-D spectrum taking a window that only includes the central source and leaves the negative features outside. However, in the context of GN 42912, we can see that these "holes" fall very close to the central emission clumps and may impact the final extraction.

To overcome this issue, we implemented a manual background estimation based on a most simplistic strategy: a sliding window of limited height and width measurement the typical background estimated in this feature-free (cutting all pixels above 5σ of the standard deviation) range. In this work, we used a sliding window of height 3 pixels and width 20 pixels on both side on the pixel considered. The relatively small height is chosen to avoid the impact of including pixels impacted by different bar shadows effects (horizontal bars where the global background may significantly differ from each other) in the median values. Each pixel in the data is replaced by the median value within this window, efficiently cutting too bright pixels. The approach is applied to all slits, such that the final background subtracted to the data is the mean of the individual backgrounds estimated from each slit.

The second panel of A1 shows the final 2d spectrum, centered on [O III 5008Å], after applying this strategy (referred to as the Median BG solution). It highlights that we recovered the more extended part of the emission profiles which may have been removed in the case of the Nodding-based background approach. The third panel shows the differences between both first and second panels. Largest differences are, expectedly, where the nodding strategy actually remove the central source, but we also observe small differences in the center of the 2-D spectrum, suggesting this new background solution affects the central source. The fourth panel shows the difference in the final 1-D spectrum of the [O III 5008Å] emission lines (continuum subtracted). The spectrum recovered shows slightly more flux with the new approach, which is consistent with the face that we have been able to recover flux which is subtracted by the default approach. Note that these differences are marginal, and remain with the uncertainties so that using either approach would not significantly impact the flux values shown in 2. Further, this modified background approach is mostly impactful for the brightest lines, namely the [O III] and Hβ. For fainter, less extended lines such as [O II] and Mg II, this does not impact the final extraction.

Finally, and importantly, the window size and sigma cutoff have been manually optimized to perform well in the context of this particular observations. This is not a semi-automatic method, which means that these parameters must likely be tuned depending on the data considered. The modified MSAEXP package is available upon request.

This paper has been typeset from a TEX/LATEX file prepared by the author.

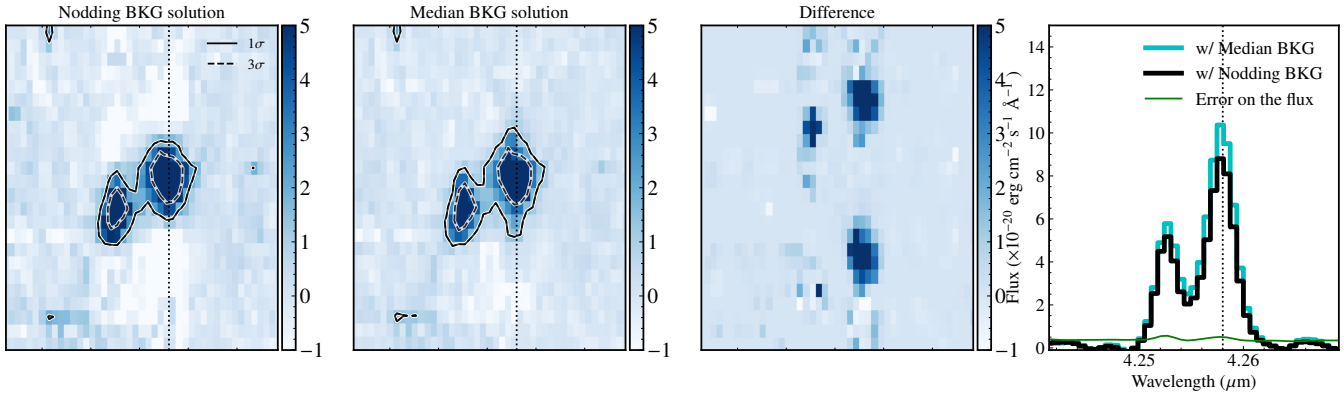

Figure A1. Comparison the different background subtraction method used for the reduction of the G235H and G395H data. The left panel shows the final 2-D spectrum, centered on the [O III] 5008Å line, after using the default background subtraction based on the three-nod pattern. Significant negative flux regions surround the two bright clumps. The second panel shows the same final 2-D spectrum after using a median-based background solution. The overall 2-D spectrum is smoother and the emission lines are slightly more extended than seen in the previous panel. The third panel simply displays the difference between the two first panels, and the fourth, most right panel shows the difference on the final extracted 1-D spectrum. We note a slightly larger amount of flux with the new reduction used in this work, yet we note that we found that these differences are marginal and do not significantly influence the final results.